

See discussions, stats, and author profiles for this publication at: <https://www.researchgate.net/publication/7059543>

Experimental and ab Initio Study of the HO₂·CH₃OH Complex: Thermodynamics and Kinetics of Formation †

ARTICLE *in* THE JOURNAL OF PHYSICAL CHEMISTRY A · JULY 2006

Impact Factor: 2.69 · DOI: 10.1021/jp056579a · Source: PubMed

CITATIONS

24

READS

54

5 AUTHORS, INCLUDING:



Mitchio Okumura

California Institute of Technology

133 PUBLICATIONS 3,025 CITATIONS

SEE PROFILE



Jaron C Hansen

Brigham Young University - Provo Main Cam...

37 PUBLICATIONS 354 CITATIONS

SEE PROFILE

Experimental and ab Initio Study of the HO₂•CH₃OH Complex: Thermodynamics and Kinetics of Formation[†]

Lance E. Christensen[‡] and Mitchio Okumura*

Arthur Amos Noyes Laboratory of Chemical Physics, Division of Chemistry and Chemical Physics, California Institute of Technology, Pasadena, California 91125

Jaron C. Hansen[§] and Stanley P. Sander*

Jet Propulsion Laboratory, California Institute of Technology, Pasadena, California 91109

Joseph S. Francisco

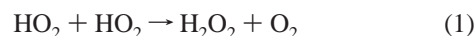
Departments of Chemistry and Earth and Atmospheric Sciences, Purdue University, West Lafayette, Indiana 47906-1393

Received: November 14, 2005; In Final Form: February 1, 2006

Near-infrared spectroscopy was used to monitor HO₂ formed by pulsed laser photolysis of Cl₂–O₂–CH₃–OH–N₂ mixtures. On the microsecond time scale, [HO₂] exhibited a time dependence consistent with a mechanism in which [HO₂] approached equilibrium via HO₂ + CH₃OH \xrightleftharpoons{M} HO₂•CH₃OH (3, –3). The equilibrium constant for reaction 3, *K_p*, was measured between 231 and 261 K at 50 and 100 Torr, leading to standard reaction enthalpy and entropy values (1 σ) of Δ_r*H*_{246K}^o = –37.4 ± 4.8 kJ mol^{–1} and Δ_r*S*_{246K}^o = –100 ± 19 J mol^{–1} K^{–1}. The effective bimolecular rate constant, *k*₃, for formation of the HO₂•CH₃OH complex is 2.8^{+7.5}_{–2.0}•10^{–15}•exp[(1800 ± 500)/*T*] cm³ molecule^{–1} s^{–1} at 100 Torr (1 σ). Ab initio calculations of the optimized structure and energetics of the HO₂•CH₃OH complex were performed at the CCSD(T)/6-311++G-(3df,3pd)/MP2(full)/6-311++G(2df,2pd) level. The complex was found to have a strong hydrogen bond (*D_e* = 43.9 kJ mol^{–1}) with the hydrogen in HO₂ binding to the oxygen in CH₃OH. The calculated enthalpy for association is Δ_r*H*_{245K}^o = –36.8 kJ mol^{–1}. The potentials for the torsion about the O₂–H bond and for the hydrogen-bond stretch were computed and 1D vibrational levels determined. After explicitly accounting for these degrees of freedom, the calculated Third Law entropy of association is Δ_r*S*_{245K}^o = –106 J mol^{–1} K^{–1}. Both the calculated enthalpy and entropy of association are in reasonably good agreement with experiment. When combined with results from our previous study (Christensen et al. *Geophys. Res. Lett.* **2002**, 29; doi: 10.1029/2001GL014525), the rate coefficient for the reaction of HO₂ with the complex, HO₂ + HO₂•CH₃–OH, is determined to be (2.1 ± 0.7) × 10^{–11} cm³ molecule^{–1} s^{–1}. The results of the present work argue for a reinterpretation of the recent measurement of the HO₂ self-reaction rate constant by Stone and Rowley (*Phys. Chem. Chem. Phys.* **2005**, 7, 2156). Significant complex concentrations are present at the high methanol concentrations used in that work and lead to a nonlinear methanol dependence of the apparent rate constant. This nonlinearity introduces substantial uncertainty in the extrapolation to zero methanol.

I. Introduction

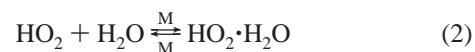
The HO₂ radical is an important intermediate in combustion and atmospheric chemistry, and its self-reaction



is the primary source of H₂O₂ in the stratosphere and the upper troposphere. In the troposphere, H₂O₂ catalyzes the oxidation of S(IV) to S(VI) after heterogeneous uptake in aerosol particles.¹ In the stratosphere, H₂O₂ is a temporary reservoir for HO_x radicals and therefore plays a role in HO_x-catalyzed

ozone depletion. Because H₂O₂ in the stratosphere is in steady state with its production step (reaction 1) and removal step (photolysis), measurements of H₂O₂ by remote sensing instruments on high-altitude balloons and spacecraft provide a means to infer local concentrations of HO₂.² These measurements, in conjunction with measurements of OH now available from space from the Microwave Limb Sounder (MLS) instrument onboard the EOS-Aura satellite, will provide important constraints on the global budget of stratospheric HO_x radicals.³

Hamilton first demonstrated that the HO₂ self-reaction rate is enhanced in the presence of H₂O.⁴ He suggested that this enhancement was a result of the formation of a reactive complex between HO₂ and H₂O



Since then, numerous investigations have substantiated and

[†] Part of the special issue “David M. Golden Festschrift”.

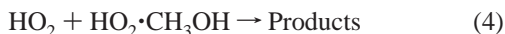
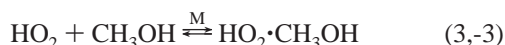
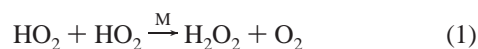
* To whom correspondence should be addressed. Stanley.P.Sander@jpl.nasa.gov and mo@its.caltech.edu.

[‡] Current address: Jet Propulsion Laboratory, Pasadena, CA 91109.

[§] Current address: Department of Chemistry, Brigham Young University, Provo, UT 84602.

quantified this phenomenon^{5–9} and shown that NH₃^{5,10} and CH₃-OH^{1,2,11,12} enhance the rate as well. Additionally, studies have demonstrated that the rate of HO₂ + NO₂ is enhanced by H₂O and CH₃OH.^{13,14}

In the kinetics studies cited above, the enhancement has been attributed to the formation of a reactive hydrogen-bonded complex, HO₂•X, where X = H₂O, NH₃, or CH₃OH. In the case of methanol enhancement of the HO₂ self-reaction, the overall mechanism can be described as



The self-reaction rate coefficient, k_1 , has bi- and termolecular contributions, $k_1 = k_0 + k'[M]$. We denote the equilibrium constant for reaction 3 in concentration (cm^{−3}) and pressure (atm^{−1}) units as K_c and K_p , respectively.

A key assumption at high pressure and low radical concentration is that the complex thermalized and is not a short-lived energized transient species. It is further assumed that equilibrium is established on a much shorter time scale than the rate of HO₂ loss due to reactions 1, 4, and 5. These assumptions are based, in part, on the observation that HO₂ loss follows second-order kinetics despite the presence of rate-enhancing species. The present investigation will provide new kinetic evidence supporting these assumptions.

Though much of the evidence for the existence of HO₂•X complexes has come from kinetic studies, other evidence exists. Aloisio et al.¹⁵ measured the extent of gas-phase HO₂ complexation with water vapor using discharge-flow/FTIR spectroscopy and determined the equilibrium constant for the formation of HO₂•H₂O. Nelander acquired the infrared spectrum of matrix-isolated HO₂•H₂O and argued that the complex, under matrix conditions, is cyclic in nature in which both ends of HO₂ participate in hydrogen bonds.¹⁶ Ab initio calculations predict that HO₂ forms hydrogen-bonded complexes with a number of polar molecules, with HO₂ as the proton donor.^{17,18} Currently, there are no published theoretical studies of the HO₂•CH₃OH complex.

The H₂O dimer, which has been extensively studied, provides a useful reference point in studies of the thermodynamics of HO₂ complexes. Curtiss et al.¹⁹ experimentally determined ΔH_{assoc} of the H₂O dimer to be (-15.0 ± 2.1) kJ mol^{−1} between 358 and 386 K. Feyereisen et al.²⁰ used ab initio calculations to determine a value of ΔH_{assoc} of (-13.4 ± 0.4) kJ mol^{−1} at 375 K. Both experimental and ab initio evidence indicate that HO₂ complexes have larger values of ΔH_{assoc} than the water dimer. This is not surprising, as HO₂ is a much stronger acid than water and should therefore be an excellent proton donor in a hydrogen-bonded complex ($\Delta_{\text{acid}}G(\text{HCl}) = 1373$ kJ mol^{−1}, $\Delta_{\text{acid}}G(\text{HO}_2) = 1450$ kJ mol^{−1}, $\Delta_{\text{acid}}G(\text{H}_2\text{O}) = 1605$ kJ mol^{−1}).²¹ The strong hydrogen bonds in these HO₂ complexes, with ΔH_{assoc} values typically 30–60 kJ mol^{−1}, result in substantial complex formation at modest concentrations ($<10^{16}$ molecules cm^{−3}) of water and methanol.

The methanol complex, HO₂•CH₃OH, is of particular importance, because methanol is frequently used as a precursor for HO₂ in laboratory experiments. Andersson et al. were the first to demonstrate that methanol enhanced the rate of the HO₂ self-

reaction.¹¹ In more recent work from this laboratory, Christensen et al.² examined the effects of methanol at lower temperatures and pressures than Andersson et al. By systematically varying the methanol concentration, and by using an HO₂ source that did not use methanol, Christensen et al. found that previous studies did not take into account the influence of methanol on measured values of k_1 . This led to errors as large as a factor of 2 at temperatures relevant to the upper troposphere and lower stratosphere (<240 K). These errors were also reflected in the recommendations for k_1 in rate constant evaluations used in atmospheric modeling studies. Bloss et al.¹² were the first to report values of K_c . They determined $K_c(298 \text{ K})$ by measuring the methanol enhancement of the HO₂ self-reaction.

Recently, Stone and Rowley have reported measurements of the rate enhancement of the HO₂ self-reaction by both water and methanol from 236 to 309 K.²² These studies were conducted at 760 Torr (at 296 K, the pressure dependence was measured between 100 and 760 Torr and found to be consistent with earlier results). In these experiments, HO₂ was formed using methanol as a precursor. The authors extrapolated their measurements in the presence of methanol to zero methanol, and determined a temperature-dependent self-reaction rate constant k_1 at 760 Torr in the absence of methanol. Their findings disagree with the results of Christensen et al. even after taking into account differences in the total pressure between the two studies. In particular, they find that the rate coefficient k_1 for the HO₂ self-reaction is significantly higher at lower temperatures. The discrepancy in k_1 has an impact on atmospheric modeling of HO_x chemistry in the atmosphere and the predicted abundance of H₂O₂. One possible source of disparity lies in the relatively high concentrations of methanol (up to 4×10^{17} cm^{−3}) used in the Stone and Rowley experiments. Despite using such large concentrations, these authors assumed the low concentration limit in their analysis. Knowledge of the equilibrium constant for complex formation, reaction 3, would allow an assessment of the validity of their analysis and hence the accuracy of their k_1 determination.

In this paper, we report measurements of HO₂ kinetics in the presence of excess CH₃OH on time scales that are short compared with that of the self-reaction of HO₂. Under these conditions, we could observe the temporal behavior of HO₂ as it complexed with methanol and relaxed to equilibrium (reaction 3). We have measured the equilibrium constant K_p and association rate coefficient k_3 for the formation of the HO₂•CH₃OH complex between 231 and 261 K at 50 and 100 Torr. From the temperature dependence of K_p , $\Delta_r H_{246\text{K}}^\circ$ and $\Delta_r S_{246\text{K}}^\circ$ were determined for the association of HO₂ and methanol to form HO₂•CH₃OH. Reverse rate coefficients k_{-3} were inferred. Ab initio calculations of the binding energy and structure of the complex were performed, and theoretical values for $\Delta_r H_{245\text{K}}^\circ$ and $\Delta_r S_{245\text{K}}^\circ$ were determined. Portions of the intermolecular potential surface were mapped out to examine the floppiness of the complex.

II. Methods

II.A. Experimental Methods. The IR kinetic spectroscopy (IRKS) apparatus has been described in detail elsewhere.¹⁴ Briefly, a 308-nm, 100-mJ/pulse excimer laser was used to photolyze Cl₂ in the presence of CH₃OH and O₂ to generate HO₂. The concentration of HO₂ within the analysis region was monitored in the near-IR by wavelength-modulated diode laser spectroscopy.

The analysis region was contained within the reaction cell, a 165-cm-long Pyrex cylinder with an inner diameter of 5 cm. Precooled reagent gases entered the center of the reaction cell

and flowed toward two outlet ports on each end. By controlling the temperature of liquid methanol contained within a jacket surrounding the reaction cell, the temperature of the reagent gases was regulated. The reaction cell was supported on both ends by aluminum chambers. Each aluminum chamber contained a CaF_2 window permitting the entry and exit of analysis and photolysis beams, a spherical gold-plated mirror, and an inlet for dry N_2 purge gas. The purge gas flowed from the aluminum chambers toward the gas outlet ports. In addition to protecting the optics, this flow design confined the reagent gas to the region between the gas exit ports. The total length in which the reagent gas resided was 137 ± 1 cm.

The excimer photolysis beam (2 cm wide, 1 cm high) passed once through the length of the reaction cell. The photolysis volume, defined as the region in which the photolysis beam and the reagent chemicals overlapped, was a rectangular volume $2 \text{ cm} \times 1 \text{ cm} \times (137 \pm 1) \text{ cm}$ in the middle of the cell.

The near-IR probe beam was emitted from a distributed feedback (DFB) diode laser. The beam passed through a hole in one of the spherical gold mirrors. The mirrors (radius of curvature = 203.2 cm) were separated by 182 cm and oriented so that they formed a Herriott cavity that folded the near-IR beam so that it was multipassed through the photolysis volume 30 times. Since one of the mirrors was placed above the path of the photolysis beam and one of the mirrors was placed below, the total path length of near-IR beam through the photolysis volume was nontrivial to measure. From visual inspection, the path length was estimated to be 2000 cm. Since these experiments did not require the exact path length, further refinement of this measurement was not pursued.

The emission wavelength of the diode laser was modulated at 6.8 MHz by sinusoidally modulating the input current to the diode laser. 2f-Heterodyne detection was employed. The diode laser probed a group of blended rovibrational HO_2 transitions near 6638.2 cm^{-1} associated with the OH overtone stretch ($2\nu_1$) and nominally assigned to the $^9\text{Q}_2$ band head. The near-IR signal was not affected by species other than HO_2 . Experiments where HCl , H_2O_2 , and CH_2O were flowed directly into our reaction cell demonstrated that these species did not contribute to our near-IR signal. Further, no significant differences in measured rate parameters for the HO_2 self-reaction were observed using three distinct rovibrational HO_2 transitions between 6625 and 6638.2 cm^{-1} . Methanol absorbs weakly in this spectral region, and its 2f signal was determined to be less than 0.5% of our typical signal at 6632.8 cm^{-1} . We found no evidence for absorption by $\text{HO}_2 \cdot \text{CH}_3\text{OH}$ at 6638.2 cm^{-1} , nor was it expected. Hydrogen bonding typically decreases the intensity of overtone transitions and also results in a red shift of their transition frequencies of several hundred wavenumbers.²³ Ab initio calculations have indicated that, for the $\text{HO}_2 \cdot \text{H}_2\text{O}$ complex, a red shift of around 300 cm^{-1} is expected for the OH stretch fundamental of HO_2 .²⁴ Similarly, the OH overtone band of HO_2 in the $\text{HO}_2 \cdot \text{CH}_3\text{OH}$ complex is likely shifted completely out of the frequency range of the diode laser.

A battery-powered, SRS SR560 low-noise preamplifier with a low-pass filter amplified the demodulated signal. The preamplifier circuitry had an inherent low-pass bandwidth of $\sim 2 \text{ MHz}$ (3 dB point) and introduced a time delay of $\sim 500 \text{ ns}$. Signal from a photodiode monitoring the excimer laser radiation triggered the data acquisition card. After amplification, the signal was digitized to 16 bits of precision (effective precision of 14 bits) by a Gage Compuscope 1602 data acquisition card. For measurements of the equilibrium constant and the association and dissociation rates of the $\text{HO}_2 \cdot \text{CH}_3\text{OH}$ complex, data were

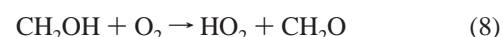
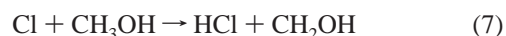
TABLE 1: Experimental Conditions and Ranges of Reagent Concentrations

T K	P Torr	$[\text{Cl}_2]$ 10^{14} cm^{-3} 99.5%	$[\text{O}_2]$ 10^{18} cm^{-3} 99.996%	$[\text{CH}_3\text{OH}]$ 10^{16} cm^{-3} HPLC	$[\text{N}_2]$ 10^{18} cm^{-3} 99.993%
231	50	30–33	0.9–1.5	0.5–2.4	0.9–1.5
231	100	5.4–7.1	1.6	0.3–2.2	1.6
240	100	4.3–9.1	2.7–3.5	1.4–9.1	0–0.8
251	100	6.1–9.6	2.2–3.4	5.1–28	0–1.2
261	100	4.3–14	2.2–3.3	4.5–33	0–1.1

sampled at the highest rate possible, 2.5 Msa s^{-1} for a sampling time interval of 400 ns. The combination of sampling rate and low-pass bandwidth was not ideal because of possible aliasing. The bandwidth was chosen because, at the time, the next highest available low-pass frequency was 1 MHz; it was deemed more important to prevent low-pass bandwidth distortions of the HO_2 decay signal than to prevent noise from aliasing. The sensitivity of the instrument toward measuring $[\text{HO}_2]$ was ca. $4 \cdot 10^8$ molecules cm^{-3} in a 1-Hz bandwidth.

UV spectroscopy was employed to calibrate the near-IR signal. Light from a deuterium lamp (Hamamatsu, 150 W) was collimated, then passed once through the length of the photolysis region, and finally entered an Acton SpectraPro-300i monochromator (1200 grooves mm^{-1} , 0.3 m) with a mounted photomultiplier tube (PMT). The total path length was 137 ± 1 cm. The monochromator was set to 220 nm, and the total absorbance measured. Formation of HO_2 was achieved via photolysis of $\text{F}_2\text{--H}_2\text{--O}_2\text{--N}_2$ reagent gases. These reagents were employed to prevent complications arising from absorption from $\text{HO}_2 \cdot \text{CH}_3\text{OH}$, which is expected to have a UV cross-section similar to that of HO_2 .²⁵ Absorbance due to H_2O_2 was accounted for. By comparing the rates of $\text{HO}_2 + \text{HO}_2$ in the UV and near-IR, the near-IR probe signal was calibrated. This is described in greater detail elsewhere.¹⁴ It should be noted that experimental values of K_p , k_3 , and k_{-3} derived in the present work are not dependent upon calibration of the near-IR signal, because their values depend only on relative changes in HO_2 signals at various methanol concentrations. Calibration was performed solely to add confidence in the interpretation of our results.

For all experiments except calibration of the near-IR signal, HO_2 was generated by photolysis of $\text{Cl}_2\text{--CH}_3\text{OH--O}_2\text{--N}_2$ gas mixtures by the reactions



The concentration ranges and purities of the reactants are listed in Table 1. The concentrations of O_2 and CH_3OH were sufficiently high in comparison to other reactive species so that they could be considered constant. $[\text{CH}_3\text{OH}]$ was varied by changing the N_2 flow rate through a bubbler containing liquid methanol. The bubbler was immersed in a bath maintained within $\pm 1^\circ \text{C}$ of the set point. To determine the concentration of methanol within the reaction cell, the NIST vapor pressure for methanol was utilized,²¹ and it was assumed that the N_2 exiting the bubbler was saturated with methanol. After the completion of this work, comparisons were made between methanol concentrations in the reaction cell calculated assuming bubbler saturation and in situ UV absorption measurements using a photometer at 184.9 nm.²⁶ The two methods agreed to

within 10%, provided the bubbler pressure was larger than 300 Torr. This condition applied for most of the experiments reported here.

All Cl atoms produced by photolysis were assumed to form HO_2 . Complications from the $\text{Cl} + \text{HO}_2$ reaction were negligible because of the relatively high methanol concentration and large value of k_7 . For this assessment, the kinetics modeling program *FACSIMILE*²⁷ was employed, and the values of k_7 , k_8 , and the rate constant for $\text{Cl} + \text{HO}_2$ were taken from the NASA data evaluation.²⁸ The $\text{HO}_2 + \text{CH}_2\text{OH}$ reaction was assumed to be insignificant because of high O_2 concentration and large k_8 value. We modeled the possible rate enhancement due to complexes of HO_2 with secondary products CH_2O and H_2O_2 , assuming the same rate coefficient as $\text{HO}_2 + \text{HO}_2 \cdot \text{CH}_3\text{OH}$ derived after measuring K_p and inferring k_4 from earlier work.² The calculated enhancement due to these secondary product complexes was negligible; at 231 K, 100 Torr, the calculated effect was less than 6%.

Measurements were acquired by averaging HO_2 signals from 50 consecutive excimer shots. The period between excimer shots was set to equal the residence time in the reaction cell (2.5–5 s).

II.B. Computational Methods. Calculations were performed to determine structure, energetics, and vibrational frequencies of the $\text{HO}_2 \cdot \text{CH}_3\text{OH}$ complex using both density functional theory and ab initio methods.

Optimized geometries were found with both B3LYP and MP2(full) methods. The geometries were optimized using Schlegel's method to better than 0.001 Å for bond lengths and 0.01° for bond angles, with a self-consistent field convergence of at least 10^{-8} on the density matrix. The residual force was less than 10^{-4} atomic units. Vibrational frequencies, intensities and zero-point vibrational energies were calculated at the B3LYP and MP2(full)/6-311++G(2d,2p) level using the optimized geometry found at the same theory/basis set combination. Further refinement in energies for all species involved in the $\text{HO}_2 \cdot \text{CH}_3\text{OH}$ complex were performed using single-point calculations at the CCSD(T)/6-311++G(2df,2pd) and CCSD(T)/6-311++G(3df,3pd) levels for the optimized geometry found at the MP2(full)/6-311++G(3df,3pd) level.

The expectation value $\langle s^2 \rangle$ was monitored for the open-shell species, HO_2 and $\text{HO}_2 \cdot \text{CH}_3\text{OH}$ species. The expectation value was never found to exceed 0.76 before spin annihilation. After spin annihilation, the value of $\langle s^2 \rangle$ was found to be 0.75, the correct value for a pure doublet. The wave functions were thus not contaminated by higher-multiplicity states in any of these calculations.

III. Results

III. A. Experimental Measurements of K_p , k_3 , and, k_{-3} . The time-dependence of $[\text{HO}_2]$ was recorded over the first 1.5 ms after an excimer photolysis pulse. To determine the values of K_p , k_3 , and, k_{-3} , data acquired within the first 50 μs were analyzed. Data acquired after 50 μs were used to put an upper limit on the rate of HO_2 loss due to reactions 1, 4, and 5. At a particular temperature and pressure, data were collected at four to six different methanol concentrations. Each such set of measurements constituted an experimental run. At 231 K, two experimental runs were done at 100 Torr and one experimental run was done at 50 Torr. For the temperatures 240, 251, and 261 K, three experimental runs were done at each temperature, all at 100 Torr. All measurements were done using tunable diode, near-IR, wavelength-modulation spectroscopy, with absolute concentrations determined by UV spectroscopy, as described above.

Establishing the Kinetic Mechanism. Three measurements from an experimental run at 240 K are shown in Figure 1, each

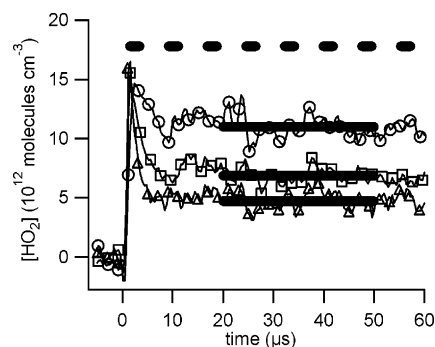


Figure 1. Time dependence of $[\text{HO}_2]$ at 240 K and 100 Torr at various methanol concentrations (thin solid lines). Data were acquired at several methanol concentrations (in molecules cm^{-3}): 2.1×10^{16} (\circ), 5.5×10^{16} (\square), 9.1×10^{16} (\triangle). The top dashed line is the sum of $[\text{HO}_2] + [\text{HO}_2 \cdot \text{CH}_3\text{OH}]$, assuming the only loss process for HO_2 was complexation. The thick lines give the final equilibrium concentration of HO_2 , $[\text{HO}_2]_{\text{eq}}$. Note that the symbols labeling the data curves are spaced five data points apart for clarity. The thin solid lines are drawn through every data point.

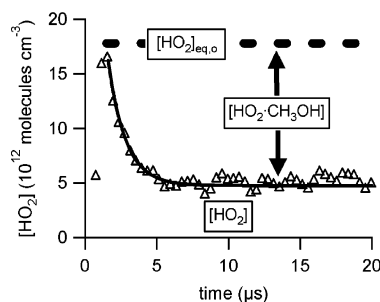


Figure 2. $[\text{HO}_2]$ signal vs time at a methanol concentration of 9.1×10^{16} molecules cm^{-3} for 240 K, 100 Torr. The plot is a magnified version of the same run displayed in Figure 1. The solid line is a fit using eq 13. Note that every data point is shown as a symbol.

acquired at a different methanol concentration. For clarity, one of the measurements depicted in Figure 1 is magnified in Figure 2. Initial HO_2 concentrations were on the order of 10^{13} cm^{-3} , orders of magnitude less than the methanol concentration. These figures demonstrate typical behavior of the $[\text{HO}_2]$ signal observed in the present study: Upon photolysis of $\text{Cl}_2\text{--O}_2\text{--CH}_3\text{OH}$ gas mixtures, $[\text{HO}_2]$ quickly rose to a peak value within a few microseconds, subsequently decayed exponentially to a nonzero value within 20 μs , and remained nearly constant between 20 μs and 50 μs . This behavior depended strongly on methanol; both the magnitude of $[\text{HO}_2]$ loss and rate of decay increased with methanol concentration.

The time dependence of $[\text{HO}_2]$ was consistent with the kinetics of $\text{HO}_2 \cdot \text{CH}_3\text{OH}$ complex formation. HO_2 was quickly generated, as all Cl atoms were converted to HO_2 within a few microseconds (at most), based on the known rate coefficients of reactions 7 and 8. HO_2 then rapidly associated with methanol by a pseudo-first-order rate law, and the HO_2 concentration decayed to a constant value as complexation approached equilibrium within 20 μs . The decay times seen in Figures 1 and 2 were far too short for radical–radical reactions such as $\text{HO}_2 + \text{HO}_2$ to contribute to the HO_2 loss at the concentrations used here. Although it was expected that the complex would have reacted much more rapidly with the HO_2 monomer, loss of HO_2 by this process should still have been minimal, even at gas kinetic rates. The observation of nearly constant $[\text{HO}_2]$ by 20 μs confirmed that reactions 4 and 5 were insignificant loss processes for HO_2 during this time period.

Once HO_2 formation was complete, the time dependence of $[\text{HO}_2]$ was then exclusively determined by complexation, with

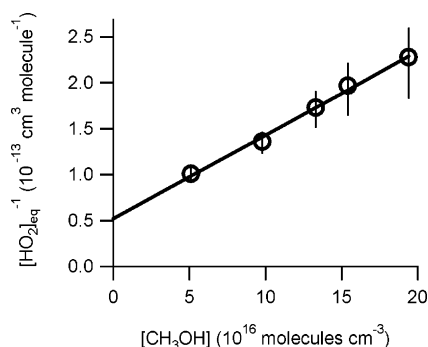


Figure 3. Measured values of $[\text{HO}_2]_{\text{eq}}^{-1}$ vs methanol concentration for one of the three experimental runs at 251 K and 100 Torr. As discussed in the text, the extrapolated value at zero methanol, $[\text{HO}_2]_0$, is equivalent to $[\text{Cl}]$ produced from photolysis, which is in turn equivalent to $[\text{HO}_2 \cdot \text{CH}_3\text{OH}] + [\text{HO}_2]$ after all Cl has been converted to HO_2 (a few microseconds after photolysis). Displayed uncertainties are 1 σ .

a first-order rate constant $k_3[\text{CH}_3\text{OH}] + k_{-3}$. To illustrate this point, a kinetic model describing an initial nonequilibrium state evolving into an equilibrium state is overlaid on the data in Figure 2. This model utilized only the peak value of $[\text{HO}_2]$ and reactions 3 and -3 . This fit will be discussed in detail below.

If equilibrium between HO_2 and the complex was established by 20 μs , then the “final” constant value of $[\text{HO}_2]$ between 20 μs and 50 μs , which we denote as $[\text{HO}_2]_{\text{eq}}$, should obey

$$K_c = \frac{[\text{HO}_2 \cdot \text{CH}_3\text{OH}]_{\text{eq}}}{[\text{HO}_2]_{\text{eq}}[\text{CH}_3\text{OH}]} \quad (9)$$

where $[\text{HO}_2]_{\text{eq}}$ and $[\text{HO}_2 \cdot \text{CH}_3\text{OH}]_{\text{eq}}$ are the equilibrium concentration of HO_2 and adduct, respectively. Let $\Delta[\text{HO}_2] = [\text{HO}_2]_0 - [\text{HO}_2]_{\text{eq}}$ be the concentration of HO_2 lost to complexation, where $[\text{HO}_2]_0$ is the initial HO_2 monomer concentration. Assuming $\Delta[\text{HO}_2] = [\text{HO}_2 \cdot \text{CH}_3\text{OH}]_{\text{eq}}$, then

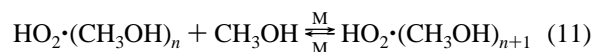
$$\frac{1}{[\text{HO}_2]_{\text{eq}}} = \frac{1}{[\text{HO}_2]_0} + \frac{K_c[\text{CH}_3\text{OH}]}{[\text{HO}_2]_0} \quad (10)$$

As shown in Figure 3 for 251 K, $[\text{HO}_2]_{\text{eq}}$ obeyed this relation, varying inversely with methanol concentration. For almost all experimental runs, this correlation was linear. Note that the total HO_2 concentration $[\text{HO}_2]_0$ is given from the linear extrapolation of $[\text{HO}_2]_{\text{eq}}^{-1}$ to zero methanol. Figure 1 shows that peak $[\text{HO}_2]$ values in the transients were observed to be between 65% and 95% of $[\text{HO}_2]_0$, but this difference was expected and attributable to the loss of HO_2 to complexation competing with HO_2 formation before the peak in HO_2 signal occurred.

At reaction times greater than 200 μs , a detectable decay in $[\text{HO}_2]$ was observed, consistent with loss by self-reaction. Between 231 and 261 K, upper limits of $2 \times 10^{-11} \text{ cm}^3 \text{ molecule}^{-1} \text{ s}^{-1}$ and $4 \times 10^{-11} \text{ cm}^3 \text{ molecule}^{-1} \text{ s}^{-1}$ were established for k_4 and k_5 , respectively, by modeling the $[\text{HO}_2]$ time dependence at these longer times and comparing with the experimental data. The modeled data were produced from the *FACSIMILE* program²⁷ using the recommended rate coefficients in NASA Evaluation Number 14.²⁸ Reactions 1 through 8 were included in the model (reaction 2 had no effect because no water vapor was present).

Thus far, we have assumed that the only product of HO_2 and CH_3OH complexation was $\text{HO}_2 \cdot \text{CH}_3\text{OH}$. In reality, further complexation is expected and may account for a significant fraction of the total HO_2 loss at sufficiently high methanol

concentrations.



Let K_n be the equilibrium constant for a value of n in reaction 11. The behavior of $\Delta[\text{HO}_2]/[\text{HO}_2]_{\text{eq}}$ with respect to methanol concentration can be described as follows:

$$\Delta[\text{HO}_2]/[\text{HO}_2]_{\text{eq}} = K_0[\text{CH}_3\text{OH}] + K_0K_1[\text{CH}_3\text{OH}]^2 + K_0K_1K_2[\text{CH}_3\text{OH}]^3 \dots \quad (12)$$

Note that $K_0 = K_c$. As stated above and shown in Figure 3, $\Delta[\text{HO}_2]/[\text{HO}_2]_{\text{eq}}$ was linear with respect to $[\text{CH}_3\text{OH}]$ for the range of methanol concentrations employed in the present study. Thus, it was concluded that further complexation was not significant and eq 12 could be truncated at the first term to eq 9, i.e., all HO_2 lost to complexation was in the form of dimer, $\Delta[\text{HO}_2] = [\text{HO}_2 \cdot \text{CH}_3\text{OH}]_{\text{eq}}$.

The equilibrium constant, K_p , can be inferred from the correlation between $[\text{HO}_2]_{\text{eq}}^{-1}$ and methanol concentration. The forward and reverse rate constants for complex formation, k_3 and k_{-3} , can be determined by measuring the rate at which $[\text{HO}_2]$ decreases from its peak value to $[\text{HO}_2]_{\text{eq}}$ and assuming that the time dependence of $[\text{HO}_2]$ is influenced only by reactions 3 and -3 . Both of these measurements are described in the next two sections.

Measurement of the Equilibrium Constant $K_p(T)$. The values of $K_p(T)$ were determined from a linear fit of $\Delta[\text{HO}_2]/[\text{HO}_2]_{\text{eq}}$ versus $[\text{CH}_3\text{OH}]$ using eq 9. At each temperature, three experimental runs were conducted, each consisting of 4 to 6 measurements of $[\text{HO}_2]_{\text{eq}}$ versus $[\text{CH}_3\text{OH}]$ for a total of 15 measurements at each temperature. For each experimental run, the value of $[\text{HO}_2]_{\text{eq}}$ at zero methanol ($[\text{HO}_2]_{\text{eq},0}$) was obtained from a linear extrapolation of $[\text{HO}_2]_{\text{eq}}^{-1}$ versus methanol concentration, as shown in Figure 3 for 251 K. The value of $[\text{HO}_2 \cdot \text{CH}_3\text{OH}]_{\text{eq}}$ was determined by subtracting $[\text{HO}_2]_{\text{eq}}$ from $[\text{HO}_2]_{\text{eq},0}$.

All measured values of $\Delta[\text{HO}_2]/[\text{HO}_2]_{\text{eq}}$ versus $[\text{CH}_3\text{OH}]$ and temperature are shown in Figure 4. The slopes of the solid lines in Figure 4 represent the average of the three experimental runs at each temperature. Values of $K_p \equiv K_c/RT$ for all experimental runs (three at each temperature) are shown in Figure 5. Typically, up to 75% of the HO_2 was complexed at the highest methanol concentrations employed at each temperature. Averaged values of $K_p(T)$ as a function of temperature are listed in Table 2.

The van't Hoff equation was used to derive $\Delta_r H_{246\text{K}}^\circ$ and $\Delta_r S_{246\text{K}}^\circ$ (246 K is the average temperature of the data set) from a weighted fit of $K_p(T)$ versus T using $K_p(T) = (RT)^{-1} \cdot \exp(\Delta_r S_{246\text{K}}^\circ/R) \cdot \exp(-\Delta_r H_{246\text{K}}^\circ/RT)$. The weights were the variance of the measured values of $K_p(T)$ for each experimental run added in quadrature with the uncertainty in T . We found $\Delta_r H_{246\text{K}}^\circ = -37.4 \pm 4.8 \text{ kJ mol}^{-1}$ and $\Delta_r S_{246\text{K}}^\circ = -100 \pm 19 \text{ J mol}^{-1} \text{ K}^{-1}$.

Determination of Rate Coefficients k_3 and k_{-3} . A subset of the kinetic data had sufficiently high signal-to-noise to permit the determination of rate constants for the formation (k_3) and decomposition (k_{-3}) of $\text{HO}_2 \cdot \text{CH}_3\text{OH}$. These runs (14 cases from a total of 60 determinations of K_p) were among those with the highest methanol concentrations, and therefore the largest values of $([\text{HO}_2]_0 - [\text{HO}_2]_{\text{eq}})$.

Pseudo-second-order and first-order values for k_3 and k_{-3} , respectively, were derived from fits to the observed HO_2 time dependences. A simplified kinetic scheme consisting of only reactions 3 and -3 was used to describe the decay of peak $[\text{HO}_2]$ to its equilibrium value, $[\text{HO}_2]_{\text{eq}}$. The time dependence of $[\text{HO}_2]$

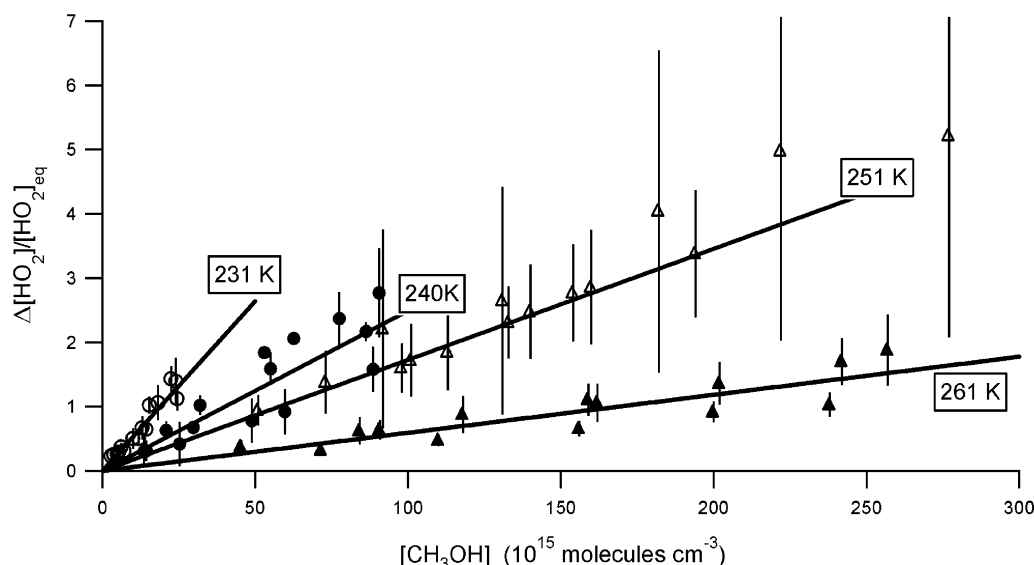


Figure 4. The dependence of $\Delta[\text{HO}_2]/[\text{HO}_2]_{2\text{eq}}$ on methanol concentration at 231 K (○), 240 K (●), 251 K (△), and 261 K (▲). The solid lines are fits to the data using eq 9. The slope of the line is $K_c(T) = RT \cdot K_p(T)$. For reference, the vapor pressures of liquid methanol at 231 and 261 K are approximately 4.6×10^{16} molecules cm^{-3} and 4.6×10^{17} molecules cm^{-3} , respectively. All measurements were conducted at less than 60% of the vapor pressure concentration at each temperature. Uncertainties are 1σ .

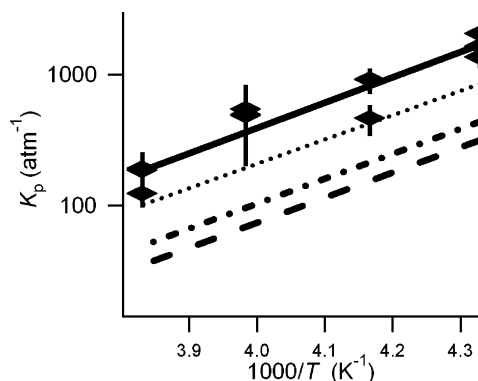


Figure 5. Van't Hoff plot of the equilibrium constant K_p for $\text{HO}_2 + \text{CH}_3\text{OH}$. Each solid diamond (◆) represents the experimental value determined for a single run. Displayed uncertainties are 1σ . The solid black line is the parametrized fit to the experimental data. The dashed line represents the theoretical harmonic values. The dashed-dotted line represents the values of K_p when the intermolecular $\text{O}'\cdots\text{H}$ stretch and torsion are treated as an anharmonic oscillator and hindered rotor, respectively. The dotted line represents the values of K_p if the remaining four modes were affected in a similar manner.

TABLE 2: Experimentally Determined K_p , k_3 , and k_{-3} for the Reaction $\text{HO}_2 + \text{CH}_3\text{OH} \rightleftharpoons \text{HO}_2\cdot\text{CH}_3\text{OH}$

T K	P Torr	K_p atm^{-1}	k_3 $10^{-12} \text{ cm}^3 \text{ s}^{-1}$	k_{-3}^a 10^5 s^{-1}	
231	50				decays
231	100	1681 ± 375	4.7 ± 1.5	0.78 ± 0.20	2
240	100	763 ± 171	7.1 ± 2.5	1.2 ± 0.5	2
251	100	506 ± 109	5.3 ± 1.5	1.7 ± 0.5	5
261	100	166 ± 37	3.2 ± 1.5	2.1 ± 1.3	3
			3.1 ± 1.0	3.7 ± 1.6	2

^a Determined from $k_3 \cdot K_c^{-1}$.

is given by

$$[\text{HO}_2] = [\text{HO}_2]_0 \frac{[\text{CH}_3\text{OH}]}{[\text{CH}_3\text{OH}] + K_c^{-1}} \{1 - \exp[-k_3 t ([\text{CH}_3\text{OH}] + K_c^{-1})]\} \quad (13)$$

where $[\text{HO}_2]_0$ represents $[\text{HO}_2]$ at $t = 0$ s. When fitting with eq

13, the values of k_3 and $[\text{HO}_2]_0$ were allowed to vary. In each fit, $[\text{CH}_3\text{OH}]$ was fixed at its experimental value. Values of K_c were fixed at the values derived in this study. The value of k_{-3} was calculated from $k_{-3} = k_3 \cdot K_c^{-1}$.

Because the digitizer time resolution (400 ns) was insufficient to capture the initial HO_2 rise following the photolysis pulse, it was not possible to fit the entire HO_2 temporal profile. Therefore, the fits included the portion of the HO_2 profile beginning with the first data point after the HO_2 peak (approximately 1.6 μs) and ending at 50 μs . Since the kinetic model did not incorporate HO_2 formation kinetics, the parameter $[\text{HO}_2]_0$ was not physically meaningful. A typical HO_2 temporal profile at 240 K and least-squares fit are shown in Figure 2.

Measured values for the effective bimolecular rate coefficients k_3 along with the calculated values for k_{-3} at different pressures and temperatures are listed in Table 2. From these data, the Arrhenius expression for the effective second-order rate constant for formation of complex at 100 Torr was determined to be $2.8^{+7.5}_{-2.0} \cdot 10^{-15} \cdot \exp[(1800 \pm 500)/T] \text{ cm}^3 \text{ molecule}^{-1} \text{ s}^{-1}$, where the stated uncertainties represent 1σ . The pressure dependence of k_3 was derived at 231 K from measurements at 50 and 100 Torr total pressure.

Determination of Rate Coefficient k_4 . The measured equilibrium constant allows us to infer the rate coefficient for reaction 4, $\text{HO}_2 + \text{HO}_2\cdot\text{CH}_3\text{OH}$, from our previous measurements² of the methanol enhancement coefficient, k'' .

In the previous study, we measured the methanol enhancement of the HO_2 self-reaction on the millisecond time scale at a total pressure of 100 Torr, from 222 to 300 K. The methanol concentration ranged from $1 \times 10^{14} \text{ cm}^{-3}$ to a maximum which depended on temperature but was no higher than $1.3 \times 10^{16} \text{ cm}^{-3}$. The observed rate constant for the methanol-enhanced HO_2 self-reaction, k_{obs} , as measured with UV spectroscopy at 220 nm, was found to have an additional contribution which varied linearly with methanol over the range studied

$$k_{\text{obs}} = k_1 + k''[\text{CH}_3\text{OH}] \quad (14)$$

with the data fit to an empirical methanol dependence rate coefficient k'' . The Arrhenius parameters for k'' at 100 Torr were determined to be $A'' = (2.5^{+5.9}_{-1.1}) \times 10^{-36} \text{ cm}^6 \text{ molecule}^{-2} \text{ s}^{-1}$

and $E_{\text{act}}'' = (-38 \pm 2) \text{ kJ mol}^{-1}$ (the lower bound in the uncertainty in A'' was incorrectly reported as -5.9).²

If it is assumed that the absorption cross-sections for HO_2 and $\text{HO}_2 \cdot \text{CH}_3\text{OH}$ are identical, then it can be shown⁵ that the kinetics follow a second-order rate law with an effective rate coefficient

$$k_{\text{obs}} = \frac{k_1 + k_4 K_c [\text{CH}_3\text{OH}] + k_5 K_c^2 [\text{CH}_3\text{OH}]^2}{(1 + K_c [\text{CH}_3\text{OH}])^2} \quad (15)$$

At sufficiently low methanol concentrations, $K_c [\text{CH}_3\text{OH}] \ll 1$, the observed rate constant will vary linearly with methanol, and eq 15 can be truncated to⁵

$$k_{\text{obs}} = k_1 + (k_4 - 2k_1)K_c [\text{CH}_3\text{OH}] \quad (16)$$

From eqs 14 and 16, $k'' = (k_4 - 2k_1)K_c$ (this has sometimes been erroneously expressed^{9,22} as $k'' \approx k_4 K_c$).

Thus, a linear dependence is expected if $K_c [\text{CH}_3\text{OH}] \ll 1$. At 231 K, Christensen et al.² employed $[\text{CH}_3\text{OH}]_{\text{max}} = 5 \times 10^{15} \text{ cm}^{-3}$; hence, $K_c [\text{CH}_3\text{OH}]_{\text{max}} = 0.25$ using the equilibrium constant determined here. Using observed values for k_1 and k'' from our previous work, we estimate $k_4 = (2.1 \pm 0.7) \times 10^{-11} \text{ cm}^3 \text{ molecule}^{-1} \text{ s}^{-1}$ at 100 Torr, when averaged over the temperature range 222–295 K, where the uncertainty represents variance in the value of $k_4(T)$. Variations in k_4 with respect to temperature are within this uncertainty, and our values of K_c are actually determined over the temperature range 230–260 K, so we cannot extract the temperature dependence of k_4 here. An estimate of $k_4(T)$ is best obtained by fitting the observed methanol dependence to eq 15; such an analysis, along with a full report of the data reported in Christensen et al.² will be reported elsewhere.

III. B. Experimental Uncertainties. In determining K_p from measurements of $\Delta[\text{HO}_2]/[\text{HO}_2]_{\text{eq}}$, the uncertainties in the determination of $[\text{HO}_2]_{\text{eq}}$ and in the extrapolated value of $[\text{HO}_2]_{\text{eq}}$ at zero methanol averaged 5% and 8%, respectively. The combined uncertainty in the vapor pressure of CH_3OH , the flow of gas through the bubbler, and the bubbler temperature was approximately 7% at all temperatures. The uncertainty in the temperature measurement was $\pm 1 \text{ K}$. Errors due to uncertainty in the calibration of the diode laser signal were divided out of eq 9, and were therefore insignificant. The total systematic error was 12–14% (1 σ). The random errors were consistent with the signal-to-noise ratios of the HO_2 absorption signals. The uncertainties in K_p given in Table 2 are the quadrature sums of the systematic and random errors.

A possible source of systematic error not accounted for in the reported values is the effect of a nonconstant value of $[\text{HO}_2]$ between 20 μs and 50 μs from reactions 4 and 5. Our calculations, discussed above, indicated that these loss processes were insignificant. The effect of including this error would be to lower estimates of $[\text{HO}_2]_{\text{eq}}$ by at most 2.5% at higher methanol concentrations relative to lower concentrations, thereby increasing the determined value of K_p by less than a few percent.

In determining k_3 and k_{-3} , systematic errors in the absolute $[\text{HO}_2]$ concentration due to uncertainty in calibrating the diode laser signal were irrelevant, because data were fit to a first-order expression, eq 13. Uncertainty (1 σ) in the fitted values of k_3 due to precision of the data ranged from 20% to 50%. These are the reported errors.

III. C. Computational Results. Geometry. Figure 6 depicts the fully optimized minimum energy structure of $\text{HO}_2 \cdot \text{CH}_3\text{OH}$ calculated at the MP2(full)/6-311++G(3df,3pd) level. A hy-

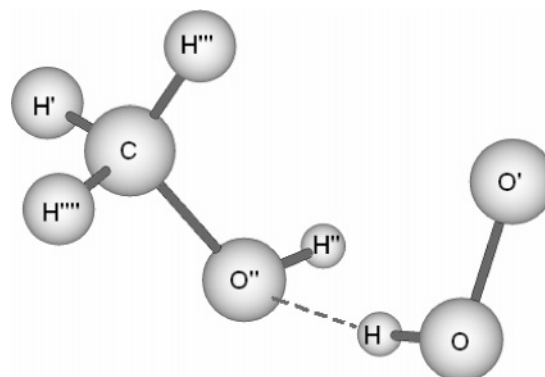


Figure 6. Optimized minimum-energy structure for the $\text{HO}_2 \cdot \text{CH}_3\text{OH}$ at the MP2(full)/6-311++G(3df,3pd) level.

drogen-bonded complex is predicted. In the primary hydrogen bond, the HO_2 acts as a proton donor with the hydrogen (H) in HO_2 binding to the oxygen (O'') in CH_3OH with a bond length of 1.686 Å. In the second, much weaker interaction, the alcoholic hydrogen (H'') in CH_3OH interacts with the lone-pair electrons on the terminal oxygen (O') in the HO_2 forming a hydrogen bond with a length of 3.224 Å and an $\text{O}'\text{H}''\cdots\text{O}'$ angle of 124°. The $\text{H}''\text{O}''\text{OO}'$ dihedral angle is 66°. The two interacting sites result in the formation of a floppy, five-membered ring. It is interesting to note that major changes are absent in the geometry of the monomer species HO_2 and CH_3OH as a result of complexation. The largest change is calculated to occur in the O–H bond length in HO_2 . In uncomplexed HO_2 , the O–H bond length is calculated to be 0.970 Å at the MP2(full)/6-311++G(3df,3pd) level. The same bond in the complex is calculated to increase by 0.02 Å to 0.990 Å. Table A, included as Supporting Information, contains the optimized geometry as a function of basis set and method.

Frequencies. Table B, included as Supporting Information, lists vibrational frequencies, intensities, and mode assignments for HO_2 , CH_3OH , and the complex calculated at the MP2(full)/6-311++G(3d,3p) level. As is typical of hydrogen-bonded complexes, the OH stretch in HO_2 is predicted to red-shift by 351 cm^{-1} from the monomer frequency of 3882 cm^{-1} upon complexation, and the intensity is predicted to increase by a factor of 17. The large shift coupled with the increased intensity makes this mode a good candidate for future experimental observation of the $\text{HO}_2 \cdot \text{CH}_3\text{OH}$ complex.

For calculations of zero-point energy and partition function, we scaled the frequencies of the complex computed at the MP2(full)/MP2(full)/6-311++G(3d,3p) level. The vibrational frequencies for HO_2 and CH_3OH were compared to those given in the HITRAN database.²⁹ An average scaling factor of 0.95 was observed (stretches and bends were not differentiated). Zero-point energies are given in Table C in the Supporting Information.

Calculated Dissociation Energies. Table 4 summarizes binding energies as a function of method and basis set. More detailed information is contained in Table C, included as Supporting Information. For both methods used for geometry optimization, the binding energy decreases as the basis set size is increased. Density functional theory (DFT) utilizing the 6-311++G(3df,3pd) basis set predicts a dissociation energy $D_e = 39.3 \text{ kJ mol}^{-1}$ and with zero-point energy correction, $D_0 = 30.9 \text{ kJ mol}^{-1}$. At the MP2(full)/6-311++G(3df,3pd) level, the electronic dissociation energy $D_e = 43.9 \text{ kJ mol}^{-1}$; using the scaled zero-point energy difference of 8.2 kJ mol^{-1} , the zero-point energy $D_0 = 37.8 \text{ kJ mol}^{-1}$, 20% larger than the DFT calculation. Single-point calculations of the energy at the CCSD(T)/6-311++G(3df,3pd) level using the MP2(full)/6-311++G(3df,-

TABLE 3: Comparison of Thermodynamic Parameters for Several Hydrogen-Bonded Complexes

complex	$\Delta_r H_T^\circ$ (kJ mol ⁻¹)	$\Delta_r S_T^\circ$ (J mol ⁻¹ K)	T (K)	method ^a
HO ₂ •CH ₃ OH	-37.4 ± 4.8	-100 ± 19	231–261	experiment (this work)
	-36.8	-106	245	CCSD(T)/6-311++G(3df,3pd) (this work)
	-25 ± 3		278–299	experiment ¹¹
HO ₂ •H ₂ O	-36 ± 16	-85 ± 40	230–298	experiment ¹⁵
	-32	-107	298	CCSD(T)/6-311++G(2df,2p) ²⁴
	-31	-103	298	HF/G(3s 1p/1s) ¹⁷
	-21.4		298	QCISD(T)/6-311++G(2d,2p) ³⁴
H ₂ O•H ₂ O	-15 ± 2	-78 ± 5	358–386	experiment ¹⁹
	-13 ± 0.4	-83.1	375	MP2,MP4,RI-MP2(FC)/aug-cc-pCVTZ* ²⁰

^a ab initio method/basis set used for energy calculations.**TABLE 4: Summary of Calculated Dissociation Energies for Dissociation of the HO₂•CH₃OH Complex and Barrier Height Energies for Internal Rotation about the O–H Bond of HO₂ (kJ mol⁻¹)^a**

method	dissociation energy			barrier height	
	D_e	ΔZPE	D_0	ΔE_{el}	ΔE_0
B3LYP/6-311++G(3df,3pd)	39.3	8.3	31.0	6.1	3.2
MP(full)/6-311++G(3df,3pd)	46.0	8.2	37.8	7.2	4.2
CCSD(T)/6-311++G(3df,3pd)/MP2(full)/ 6-311++G(3df,3pd)	43.9		35.7		

^a Harmonic frequencies were scaled by 0.95 to obtain ΔZPE . Energies were determined for geometries optimized at the given levels, except as noted for the single-point CCSD(T) energies. Zero-point energies were computed at the B3LYP/6-311++G(2d,2p) and MP2(full)/6-311++G(2d,2p) levels. Barrier geometries were partially optimized (see text).

3pd) optimized structure predict the binding energy with the scaled MP2(full) zero-point vibrational correction to be $D_0 = 35.7$ kJ mol⁻¹.

Computed Thermodynamics. The equilibrium constant, K_p , for complex formation was calculated as a function of temperature from

$$K_p(T) = \frac{Q_{\text{complex}}^\circ}{Q_{\text{HO}_2}^\circ \cdot Q_{\text{CH}_3\text{OH}}^\circ} \cdot \exp\left(\frac{D_0}{k_b T}\right) \quad (17)$$

where k_b is the Boltzmann constant, D_0 is the zero-point corrected dissociation energy, and each Q_x° ($x = \text{HO}_2$, CH_3OH , or complex) is the product of electronic, translational, rotational, and vibrational canonical partition functions referenced to the zero-point energy of each species. In addition, the complex possessed a degeneracy of two, due to the existence of two symmetric isomers distinguished by rotation about the methanol top axis. The calculated rotational constants and vibrational frequencies were used to evaluate the partition functions for both reactants HO₂ and CH₃OH as well as the complex. For these initial calculations, the vibrational partition function was computed in the harmonic oscillator approximation using the scaled MP2(full)/6-311++G(3df,3pd) frequencies.

Figure 5 shows the calculated equilibrium constant (long dashed line) over the same temperature range in which the experimental K_p was measured. The calculated equilibrium constant, K_p , is shown to decrease from a value of 153.9 atm⁻¹ at 231 K to 17.1 atm⁻¹ at 261 K. The slope of Figure 5 is $-\Delta_r H_{245\text{K}}^\circ/R$. Our computed enthalpy treating all vibrations as harmonic oscillators is $\Delta_r H_{245\text{K}}^\circ = -36.8$ kJ mol⁻¹, and the Third Law entropy is $\Delta_r S_{245\text{K}}^\circ = -111$ J mol⁻¹ K⁻¹.

The harmonic oscillator approximation is a relatively poor representation for low-frequency, large-amplitude vibrations in a hydrogen-bonded complex. In an effort to estimate the Third Law values of ΔS_T° more accurately, one-dimensional cuts of the potential energy surface along the O'•HOO' torsion angle (rotation about the OH bond of HO₂, the hydrogen bond donor) and intermolecular stretch denoted R were calculated, and then,

the contributions of these modes to the entropy change were subsequently calculated. These results are described in the following two subsections.

Torsional Potential (O'•HOO'). A one-dimensional torsional potential for internal rotation about the hydrogen bond (mode ν_{21}) was computed in order to obtain more accurate torsional energies and entropy contributions. Since the primary interacting hydrogen bond (H•••O') and the (H–O) bond of the HO₂ were nearly collinear, the internal rotation was approximated by rotating the O₂ group about the OH bond of the HO₂. The dihedral described by the atoms O'OHO'' was stepped between 0° and 360° in 10° increments, while freezing the H'''C, H'''C, and H'C bond lengths, the H'''CO'', H'CO'', and H'''CO'' bond angles, and the CO''HO dihedral angle at their optimized lowest-energy values. The latter does somewhat restrict the range of CO''O angles. The remaining degrees of freedom in the complex were allowed to relax to minimize the complex energy.

The resulting potential energy curve, calculated at the B3LYP/6-311++G(d,p) level and shown in Figure 7 (the energies in the figure are scaled down, as described below), is a single-well torsional potential with a barrier energy $\Delta E_{el} = 6.7$ kJ mol⁻¹ and, with zero-point correction, $\Delta E_0 = 3.8$ kJ mol⁻¹. At the barrier (ca. 180°), the O–O' bond points away from the methyl group H-atoms. The shoulder that arises between -60° and -120° in the calculated potential may be due to slightly repulsive interactions between the terminal oxygen (O') in HO₂ and methyl hydrogens in CH₃OH as HO₂ is rotated around the O'•••H hydrogen bond. Electrostatic and induction forces may also be important.

The height of the barrier along the torsional coordinate in Figure 7 is an indication of the strength of the secondary hydrogen bond, the interaction between the terminal O' of the HOO' and the H'' of the methanol OH group. These atoms constitute the weaker interaction of the two interacting sites in the complex. This bond is broken in the highest-energy structure, shown in Figure 8. The terminal O' atom in HO₂ is directed away from the methanol and has no interactions with any of the methanol hydrogens.

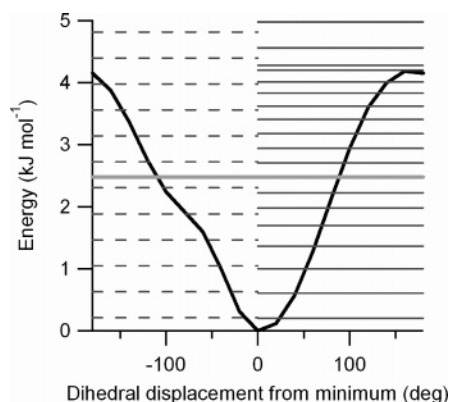


Figure 7. Torsional potential energy curve E_{el} calculated at the B3LYP/6-311++G(d,p) level for rotation of the O_2 group about the OH bond of HO_2 . Most degrees of freedom are optimized and the barrier height has been scaled to match the MP2(full) energies (see text). The dark solid line is the calculated potential as a function of the $O''HOO'$ dihedral angle being rotated between 0° and 360° . The horizontal lines on the left half are the harmonic oscillator vibrational energy levels. The horizontal lines on the right half are the torsional energy levels. The gray line through both halves represents RT at 298 K. The positive angles refer to rotation of the $O-O'$ group in the clockwise direction in Figure 6.

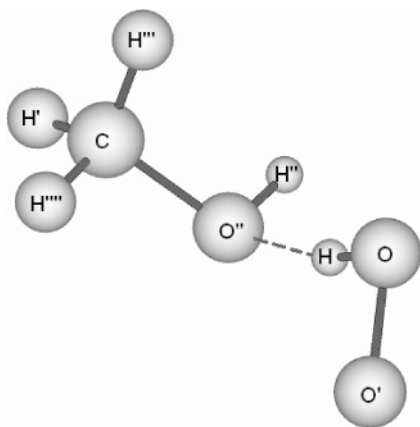


Figure 8. Geometry at the top of the O-H torsional barrier, partially optimized at the B3LYP/6-311++G(d,p) level of theory.

To refine the barrier height, the structure was optimized as a function of method and basis set, using the same method/basis set combinations that were employed in the investigation of the lowest-energy structure (though no single-point coupled-cluster calculations were performed). Differences in energy between the torsional barrier and the lowest-energy structure, corrected for zero-point energy, are shown on the right side of Table 4 and in more detail in Table C in the Supporting Information. The energy of the transition state decreases as the basis set is increased for a given method. The B3LYP calculation with the largest basis set gives a barrier height of $\Delta E_{el} = 6.1 \text{ kJ mol}^{-1}$ and, with zero-point correction, $\Delta E_0 = 3.2 \text{ kJ mol}^{-1}$, while the MP2(full)/6-311++G(3df,3pd) calculation gives a zero-point corrected barrier height of $\Delta E_0 = 4.2 \text{ kJ mol}^{-1}$, which is ca. 11% of the total binding energy calculated at the same level. The potential shown in Figure 7 has been scaled to match the MP2(full) energies.

Vibrational levels of this internal rotation were computed numerically. First, the moment of inertia was computed with the *MOIAM* program,³⁰ using the ab initio structures along the torsional path. The resulting rotational constant, $F = 63 \text{ GHz}$, was used to solve numerically for the energy levels of the scaled potential in Figure 7. The resulting energy levels are shown on the right-hand side in Figure 7, as compared to the harmonic

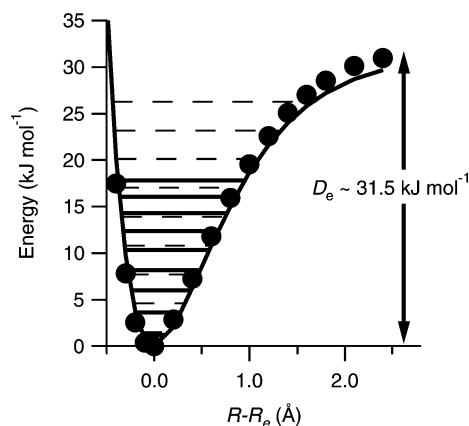


Figure 9. Slice of the potential energy surface along intermolecular hydrogen bond $R - R_e$ (the $O''\cdots H$ stretch). Single-point potential energies (●) were calculated at the B3LYP/6-311++G(d,p) level of theory and fit to a Morse potential (solid curve). The thick solid horizontal lines are the calculated anharmonic vibration energy levels for the Morse potential. The thin dashed horizontal lines are the scaled harmonic levels (258 cm^{-1}). Levels up to $\nu = 6$ are depicted.

energy levels predicted in the MP2(full) calculations shown on the left side of the figure. Spacing between the $m = 0$ and 1 torsional levels was found to be 33.7 cm^{-1} , in good agreement with the harmonic frequency of 35 cm^{-1} , but spacings between the torsional levels rapidly decreased, particularly between the shoulder and the barrier, resulting in 16 levels lying at or below the barrier energy rather than the 10 levels in the harmonic approximation.

The partition function for this mode was calculated with the hindered rotor levels to be $q_{21}(\text{hind}) = 7.4$ at 245 K and $q_{21}(\text{hind}) = 9.1$ at 300 K. In contrast, in the harmonic oscillator approximation, $q_{21}(\text{harm}) = 5.4$ at 245 K and $q_{21}(\text{harm}) = 6.5$ at 300 K. As a result, the hindered rotor model increased the entropy of the $HO_2 \cdot CH_3OH$ complex by $S_{245K} = 3.9 \text{ J mol}^{-1} \text{ K}^{-1}$ and $S_{300K} = 5.5 \text{ J mol}^{-1} \text{ K}^{-1}$.

Intermolecular Stretch ($O''\cdots H$). The $O''\cdots H$ intermolecular stretch (ν_{17}) has a harmonic frequency of 272 cm^{-1} computed at the MP2(full)/6-311++G(2d,2p) level (Table B in Supporting Information), but the low dissociation energy should lead to a fairly anharmonic potential. A one-dimensional potential curve was obtained by calculating the energy of the complex as a function of the $O''\cdots H$ bond length R . The $O''\cdots HO$ bond length of the lowest-energy optimized $HO_2 \cdot CH_3OH$ complex was stepped between 0.5 and 4.5 Å in 0.1 and 0.2 Å intervals, while allowing most of the other degrees of freedom to relax. The coordinates that remained frozen were the distances CO'' , OH , OO' , and CH'''' , the angles $O''CH''$ and $CH''''H''''$, and the dihedral angle $CH''''H''''H'$. Calculations were performed at the B3LYP/6-311++G(d,p) level of theory.

Figure 9 shows the calculated energy as a function of the displacement from the minimum-energy $O''\cdots H$ bond distance. Solid circles represent calculated potential energies, while the solid line represents the best fit to a Morse potential $V(R - R_e) = D_e[1 - e^{-\beta(R - R_e)}]^2$ using $D_e = 31.5 \text{ kJ mol}^{-1}$ and $\beta = 1.47 \times 10^8 \text{ cm}^{-1}$. For the reduced mass of this mode, results of our ab initio calculation were not used because of anharmonicity and mode coupling. Instead, the work of Xantheas and Dunning³¹ was utilized in which they observed, for the water dimer, that the MP2/6-311++G(2d,2p) calculated harmonic frequency was approximately 24% greater than the experimental frequency for the intermolecular $O\cdots O$ stretch. In the present case, to achieve an equivalent reduction between the MP2 harmonic frequency and $\omega_e - 2\omega_e x_e$ (the energy difference between $\nu =$

0 and $\nu = 1$ for the Morse potential), a reduced mass of 8.6 amu was necessary. Assuming a reduced mass of 8.6 amu, we obtained the harmonic frequency $\omega_e = 207\text{ cm}^{-1}$ and the anharmonic term $\omega_e x_e = 4.2\text{ cm}^{-1}$.

The partition function calculated using the anharmonic energy levels for the Morse potential (shown in Figure 9) is $q_{17}(\text{anh}) = 1.37$ and 1.52 at 245 and 300 K , respectively. Treating this mode as a harmonic oscillator of frequency 272 cm^{-1} yielded a partition function of $q_{17}(\text{harm}) = 1.25$ and 1.37 . The entropy of the Morse oscillator is $1.0\text{ J mol}^{-1}\text{ K}^{-1}$ greater than the entropy of the harmonic oscillator model at both 245 and 300 K . Thus, the partition function and hence the calculated entropy of the complex differ noticeably if this mode is treated as a one-dimensional anharmonic oscillator.

III. D. Entropy of the Complex. More accurate treatment of both the internal rotation about the hydrogen bond and the intermolecular stretch increased the entropy of complexation, leading to final values of $\Delta_r S_{245\text{K}}^\circ = -106\text{ J mol}^{-1}\text{ K}^{-1}$ and $\Delta_r S_{300\text{K}}^\circ = -104\text{ J mol}^{-1}\text{ K}^{-1}$ and concomitant values of $\Delta_r H_{245\text{K}}^\circ = -36.4\text{ kJ mol}^{-1}$ and $\Delta_r H_{298\text{K}}^\circ = -36.5\text{ kJ mol}^{-1}$. The equilibrium constant K_p increases by a factor of 1.4 at 245 K relative to the harmonic oscillator approximation, and the resulting van't Hoff curve is shown in Figure 5 as a dashed-dotted line.

The HO torsion and the hydrogen bond stretch represent the lower and upper frequency limits of the six low-frequency intermolecular vibrations. We expect that the remaining four intermolecular vibrations would have anharmonic corrections to their respective partition functions intermediate between these two limits. If we assume that the corrections are the geometric mean of the correction factors for the torsion and stretch modes computed above, we find that the final values are $\Delta_r S_{245\text{K}}^\circ = -98\text{ J mol}^{-1}\text{ K}^{-1}$ and $\Delta_r S_{300\text{K}}^\circ = -93\text{ J mol}^{-1}\text{ K}^{-1}$ with concomitant adjusted enthalpies of $\Delta_r H_{245\text{K}}^\circ = -35.6\text{ kJ mol}^{-1}$ and $\Delta_r H_{300\text{K}}^\circ = -35.9\text{ kJ mol}^{-1}$. The resultant K_p van't Hoff curve with corrected entropy contributions for all six modes is shown in Figure 5 as a dotted line.

IV. Discussion

IV. A. Comparison between Theory and Experiment. The experimental measurements of the equilibrium constant and association kinetics and the theoretical calculations provide consistent quantitative evidence for formation of the HO₂•CH₃OH complex. The experimental determination of $\Delta_r H_{246\text{K}}^\circ = -37.4 \pm 4.8\text{ kJ mol}^{-1}$ is in good agreement with our theoretical prediction of $\Delta_r H_{245\text{K}}^\circ = -36.8\text{ kJ mol}^{-1}$. The magnitude of these values (compared with $\Delta_r H_{358-386\text{K}}^\circ$ for water dimer formation of -15.0 kJ mol^{-1})¹⁹ indicates the presence of a strong hydrogen bond. Table 3 lists our calculated and measured binding energies compared with that for similar species.

Though the experimental and theoretical values of $\Delta_r H^\circ$ are in good agreement, there is some disparity in the experimental Second Law entropy and the computed Third Law entropy. However, this is not unexpected. Treatment of the entropy of the theoretical complex is not straightforward. Statistical treatment of low-frequency vibrational modes (harmonic oscillator, hindered rotor, or free rotor) as well as effects of anharmonicity can lead to wide variations in calculated entropy.

Using only scaled harmonic frequencies, $\Delta_r S_{245\text{K}}^\circ = -111\text{ J mol}^{-1}\text{ K}^{-1}$, and K_p underestimates experimental values by a factor of 5.4 throughout the temperature range $231\text{--}261\text{ K}$ as shown in Figure 5. Treating just two of the intermolecular vibrations explicitly reduces the entropy change to $\Delta_r S_{245\text{K}}^\circ = -106\text{ J mol}^{-1}\text{ K}^{-1}$ and brings K_p to within a factor of 3.0 .

For the intermolecular stretch ν_{17} , differences in vibrational frequencies between the MP2 harmonic calculation and the Morse potential fit to the explicit one-dimensional potential energy slice are not surprising. Xantheas and Dunning³² have done ab initio calculations of the water dimer vibrational frequencies. They show that MP2/6-311++G(2d,2p) calculations predict harmonic frequencies about 24% greater than experimental results for the O•••O stretch and nearly 40% higher for the acceptor bend (adjusting for isotopic substitution of the harmonic ab initio frequency).

It is likely that potential energy surfaces along the next four lowest-frequency modes (torsions and low-frequency bends) are also relatively flat and anharmonic. The partition function for each of these modes is significantly larger than predicted by the harmonic oscillator approximation, resulting in a further increase of calculated entropy of complexation.

The observed effective bimolecular rate coefficient k_3 for association is in the range of typical association rates in the 100 Torr range. The negative activation energy, $E_{\text{act}} = -22 \pm 6\text{ kJ mol}^{-1}$, is consistent with the complex binding energy. The rate constant at 50 Torr and 231 K is somewhat more than half that measured at 100 Torr . This result suggests that the termolecular complex association process is in the falloff region but not yet in the high-pressure limit. However, more extensive pressure-dependence study is required to verify this conclusion.

IV. B. Comparison of K_p , $\Delta_r H$, and $\Delta_r S$ with Previous Studies. The present study is the first in which the effects of HO₂ complexation with CH₃OH were directly observed. Prior studies of the association between HO₂ and CH₃OH have indirectly inferred K_p from enhancements to the apparent HO₂ self-reaction over the millisecond time scale. In one of these prior studies, Bloss et al. measured the equilibrium constant for the formation of HO₂•CH₃OH and found $K_{p,298\text{K}} = (15 \pm 2)\text{ atm}^{-1}$.¹² Extrapolation of the van't Hoff plot from the present work leads to $K_{p,298\text{K}} = (22_{-17}^{+110})\text{ atm}^{-1}$, which is consistent with the results of Bloss et al. The value of the change in enthalpy from the present study is larger than that of Andersson,¹¹ as seen in Table 3. Their value was obtained over a relatively small temperature range and, hence, is subject to a larger uncertainty.

The present results are consistent with prior experimental and theoretical examinations of a related system, HO₂•H₂O. Experimentally, Aloisio et al.^{15,24} found the equilibrium constant for HO₂•H₂O formation (K_2) to be $(5400 \pm 1400)\text{ atm}^{-1}$ at 230 K and determined an upper limit of 98 atm^{-1} at 300 K . More recently, Kanno et al.³³ determined K_2 to be $(13 \pm 8)\text{ atm}^{-1}$ at 297 K . These values are all consistent with the equilibrium constants for methanol, K_p , reported here. On the basis of their equilibrium constants, Aloisio et al. reported $\Delta_r H_{298\text{K}}^\circ = (-36 \pm 16)\text{ kJ mol}^{-1}$ and $\Delta_r S_{298\text{K}}^\circ = (-85 \pm 40)\text{ J mol}^{-1}\text{ K}^{-1}$ for the formation of HO₂•H₂O. Thus, experimental studies of the association of HO₂ with methanol and water indicate that the hydrogen bonds are similar for both complexes.

The theoretical results support this similarity. For the association of HO₂ and H₂O, Aloisio et al.^{15,24} calculated $\Delta_r H^\circ = -32\text{ kJ mol}^{-1}$ and $\Delta_r S^\circ = -107\text{ J mol}^{-1}\text{ K}^{-1}$, at the CCSD(T)/6-311++G(2df,2p)//B3LYP/6-311++G(2df,2p) level of theory in the harmonic approximation. An earlier theoretical examination of the HO₂•H₂O complex was done by Hamilton and Naleway,¹⁷ employing Hartree–Fock calculations with a Gaussian basis set [3p1p/1s]. By using the rigid rotor harmonic oscillator approximation and assuming that the entropy of the six intermolecular modes of HO₂•H₂O would be the same as that of the analogous modes in (H₂O)₂, they calculated nearly

the same values for $\Delta_r H$ and $\Delta_r S$, -31 kJ mol^{-1} and $-103 \text{ J mol}^{-1} \text{ K}^{-1}$, respectively.

Schenter et al.³¹ have shown that, for weakly bound systems such as the water dimer, calculations of thermodynamic properties are greatly complicated by the presence of quasi-bound states. Depending upon the treatment of these loosely bound states, calculations of the water dimer partition function can vary over 2 orders of magnitude between 200 and 500 K. Failing to take into account loosely bound states will result in underestimating the entropy of the complex, thereby underestimating the equilibrium constant. Our experiment records the disappearance of a specific rovibrational line of HO_2 . This observable thus leads to an empirical definition of the complex as any configuration which alters vibrational or rotational constants of HO_2 on a 10 MHz scale, and thus includes most loosely bound states. The experimentally observed K_p is therefore an upper bound. The dissociation energy of $\text{HO}_2\cdot\text{CH}_3\text{OH}$ is much larger than that for the water dimer, so the effect must be less, but nonetheless should be considered when comparing experimental and theoretical equilibrium constants.

IV. C. Comparison of k_4 with Previous Studies. We found $k_4 = (2.1 \pm 0.7) \times 10^{-11} \text{ cm}^3 \text{ molecule s}^{-1}$ at 100 Torr when averaged over the temperature range 222–295 K. This is in relatively good agreement with the measurement by Bloss et al. of $(3.2 \pm 0.5) \times 10^{-11} \text{ cm}^3 \text{ molecule s}^{-1}$ determined at 760 Torr and 298 K.

Though the present work measures the effect of methanol, it is informative to compare the present results with a recent study examining the effects of water by Kanno et al.³³ Kanno et al. determined the rate constant for $\text{HO}_2 + \text{HO}_2\cdot\text{H}_2\text{O}$ at 297 K, 50 Torr, to be $(1.5 \pm 0.1) \times 10^{-11} \text{ cm}^3 \text{ molecule}^{-1} \text{ s}^{-1}$. However, the equations used to determine k_4 and K_2 in their work are valid only if HO_2 and $\text{HO}_2\cdot\text{H}_2\text{O}$ have equivalent cross-sections. Since their near-IR signal arises from only HO_2 absorbance, the equations used to determine k_4 and K_2 in their work should be multiplied by $1 + K_2[\text{H}_2\text{O}]$. It is unclear how this would affect their final values.

The value of k_4 reported here is roughly an order of magnitude larger than k_1 , the rate coefficient for the HO_2 self-reaction itself. This result suggests that, in laboratory experiments, even a small concentration of methanol precursor can lead to significant systematic overestimation of the rate of the HO_2 self-reaction at low temperatures.

IV. D. Implications for the Rate Coefficient $k_1(T)$ for Self-Reaction. The majority of studies of the rate constant k_1 for the $\text{HO}_2 + \text{HO}_2$ self-reaction use methanol as a precursor, but only the most recent of these explicitly correct for the methanol enhancement. There is good agreement at room temperature. However, the two recent studies of Christensen et al.² and Stone and Rowley²² differ by as much as a factor of 2 in k_1 below room temperature, even after correcting for differences in total pressure. The current results on the equilibrium constant, K_p , suggest a possible explanation for the discrepancy.

In the Christensen et al.² and Stone and Rowley²² studies, HO_2 was detected by UV absorption spectroscopy. Both studies measured the dependence of the effective rate constant, k_{obs} , on methanol concentration at several temperatures and extrapolated to zero methanol to determine the self-reaction rate coefficient k_1 for each temperature. In principle, one must extrapolate k_1 from $k_{\text{obs}}(T, [\text{CH}_3\text{OH}])$ using eq 15, which is a ratio of two terms that are quadratic in $[\text{CH}_3\text{OH}]$, and in general should be nonlinear. In the limit of low methanol concentrations where complexation is negligible, i.e., $K_c[\text{CH}_3\text{OH}] \ll 1$, the effective rate constant will vary linearly with $[\text{CH}_3\text{OH}]$.

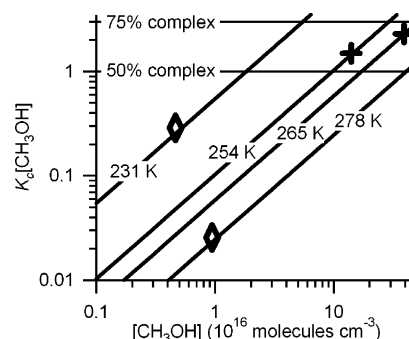


Figure 10. $K_c[\text{CH}_3\text{OH}]$ vs $[\text{CH}_3\text{OH}]$ at selected temperatures. The diamonds represent the highest methanol concentrations utilized at 231 and 278 K in the Christensen et al. study. The crosses for 254 and 265 K represent the largest methanol concentration utilized by the Stone and Rowley study. The horizontal lines are the percent of HO_2 , at a given value of $K_c[\text{CH}_3\text{OH}]$, that has been complexed, i.e., $100\% \times [\text{HO}_2\cdot\text{CH}_3\text{OH}]/([\text{HO}_2] + [\text{HO}_2\cdot\text{CH}_3\text{OH}])$.

Both studies made this assumption and fit the measured k_{obs} vs $[\text{CH}_3\text{OH}]$ to a linear dependence on methanol and extrapolated this fit to obtain k_1 for each temperature. However, Stone and Rowley²² employed relatively high concentrations of methanol with experiments performed over concentration ranges of $6 \times 10^{15} \text{ molecules cm}^{-3}$ to $4.7 \times 10^{17} \text{ molecules cm}^{-3}$ at a given temperature. These concentrations $[\text{CH}_3\text{OH}]_{\text{max}}$ were a factor of 10–50 higher than the maximum methanol concentrations used by Christensen et al., e.g., $[\text{CH}_3\text{OH}]_{\text{max}} = 1.5 \times 10^{16} \text{ molecules cm}^{-3}$ at 265 K and less at lower temperatures.

Our expression for the equilibrium constant $K_p(T)$ allows us to examine the validity of the assumption of low complex concentration in both studies. $K_c[\text{CH}_3\text{OH}]$ is plotted against $[\text{CH}_3\text{OH}]$ for several temperatures in Figure 10. Representative values of the maximum $K_c[\text{CH}_3\text{OH}]_{\text{max}}$ are plotted for both experiments. As can be seen, the experiments of Christensen et al. fall well below the $K_c[\text{CH}_3\text{OH}] = 1$ (50% complex) line; at 231 K, $K_c[\text{CH}_3\text{OH}]_{\text{max}} = 0.25$ (20% complex). The experiments of Stone and Rowley at 254 and 265 K, however, both are performed with maximum values of methanol that give $K_c[\text{CH}_3\text{OH}] = 1.5$ and 2.3, respectively (no data were given for their lowest-temperature extrapolations, at 236 and 245 K, so we cannot evaluate their estimates at those temperatures).

The Stone and Rowley experiments were thus performed over a range of methanol concentrations where the low methanol approximation does not hold, and their assumed linear extrapolation is therefore in doubt. Bloss et al.¹² observed a falloff in k_{obs} at room temperature over a similar methanol concentration range, which would arise from the denominator in eq 15, indicating that k_{obs} may well be nonlinear in the Stone and Rowley experiment. A full fit of the Stone and Rowley data to eq 15, however, seems impractical. For all temperatures below 296 K, they recorded only 5 to 6 points for each methanol dependence, while eq 15 has 3 unknowns (if the current K_p is used).

To illustrate this point, weighted fits to their data at 254 K are shown in Figure 11. Two fits are shown: a linear fit and a fit to eq 15. The rate coefficient k_1 is given by the y-intercept. The linear fit leads to a substantially higher estimate of k_1 than the full fit to eq 15, but the full fit leads to $k_1 = (4.2 \pm 7.0) \times 10^{-12} \text{ cm}^3 \text{ molecule}^{-1} \text{ s}^{-1}$, and essentially cannot determine k_1 . The approach used by Stone and Rowley, to offset the fitted line to match the lowest methanol data point(s), seems unjustified, as the deviations caused by the higher methanol concentrations are in the functional form and slope of the methanol dependence.

It is therefore unlikely that meaningful values of k_1 can be extrapolated from the results of Stone and Rowley, except

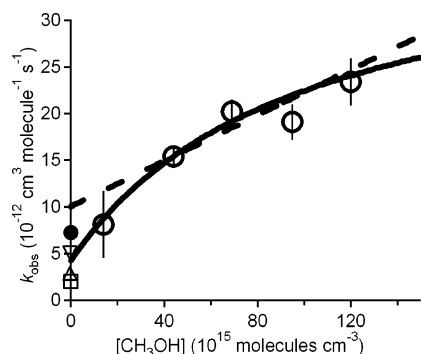


Figure 11. Comparisons of different extrapolations to the Stone and Rowley data at 254 K, 760 Torr. The data reported in their work are depicted by (O). The solid line is a weighted fit using the full equation for k_{obs} (eq 15). The dashed line is a weighted fit assuming a linear dependence. Also shown are the NASA recommended values (at zero methanol) of k_1 760 Torr (∇) and 100 Torr (\triangle) for 254 K and the value of k_1 from the Christensen et al. study at 100 Torr, 254 K, depicted as (\square). For reference, the reported value of k_1 from Stone and Rowley (760 Torr) was $(7.25 \pm 3.03) \times 10^{-12} \text{ cm}^3 \text{ molecule}^{-1} \text{ s}^{-1}$ and is depicted in the figure as (\bullet).

perhaps at 296 K. In contrast, the data of Christensen et al., measured over a range of methanol concentrations roughly 1 order of magnitude lower with higher precision, are within the linear regime and further provide a better range for extrapolation to zero methanol. A full account of those rate measurements, including consideration of the UV cross-sections for HO_2 monomer and complex (which is assumed to be identical in eq 15) and comparison with near-IR measurements, is in progress.

V. Summary

The present work confirms that the mechanism responsible for the observed rate enhancement is due to the formation of a hydrogen-bonded complex. The value of K_p for $\text{HO}_2 + \text{CH}_3\text{OH} \xrightleftharpoons{M} \text{HO}_2 \cdot \text{CH}_3\text{OH}$ and the forward and reverse rate coefficients were measured and compared with ab initio calculations. Overall, there was good agreement between experiment and theory regarding the binding energy, but experimental values of K_p were significantly larger than theoretical values. The potential energy surface of the complex was computed along the intermolecular stretch and the HO_2 torsion. The analysis presented in this work demonstrates that incorporating anharmonic effects for determining partition functions for these modes improves agreement noticeably.

Acknowledgment. This research was carried out by the Jet Propulsion Laboratory, California Institute of Technology, under contract with the National Aeronautics and Space Administration (NASA). This work was supported by the NASA Upper Atmosphere Research and Tropospheric Chemistry Programs and the NASA Graduate Student Research Program (GSRP). This research has also been supported in part by a grant from the U.S. Environmental Protection Agency National Center for Environmental Research's Science to Achieve Results (STAR) program, through grant R826236-01-0. It has not been subjected to any EPA review and therefore does not necessarily reflect the views of the Agency, and no official endorsement should be inferred. We would like to acknowledge the indispensable scientific advice of Barna László, Kyle Bayes, Brian Drouin, and Herbert Pickett, the vital technical support of Dave Natzic and Jürgen Linke, and all the exceptional work of Siamak Forouhar, Kamjou Mansour, and Sam Keo of the Microdevices Laboratory in the manufacture and testing of the diode laser. We thank David Rowley and Daniel Stone for helpful discussions of their data.

Note Added in Proof: Very recently, rotational transitions of $\text{HO}_2 \cdot \text{H}_2\text{O}$ have been observed (Suma et al. *Science* **2006**, *311*, 1278).

Supporting Information Available: Additional data on optimized structures and DFT and ab initio calculations. This material is available free of charge via the Internet at <http://pubs.acs.org>.

References and Notes

- (1) Clegg, S. M.; Abbott, J. P. D. *Atmos. Chem. Phys.* **2001**, *1*, 73.
- (2) Christensen, L. E.; Sander, S. P.; Okumura, M.; Salawitch, R. J.; Toon, G. C.; Sen, B.; Blavier, J.-F.; Jucks, K. W. *Geophys. Res. Lett.* **2002**, *29*, no. 1299.
- (3) Waters, J. W.; Read, W. G.; Froidevaux, L.; Jarnot, R. F.; Cofield, R. E.; Flower, D. A.; Lau, G. K.; Pickett, H. M.; Santee, M. L.; Wu, D. L.; Boyles, M. A.; Burke, J. R.; Lay, R. R.; Loo, M. S.; Livesey, N. J.; Lungu, T. A.; Manney, G. L.; Nakamura, L. L.; Perun, V. S.; Ridenoure, B. P.; Shippony, Z.; Siegel, P. H.; Thurstans, R. P.; Harwood, R. S.; Pumphrey, H. C.; Filipiak, M. J. *J. Atmos. Sci.* **1999**, *56*, 194.
- (4) Hamilton, E. J., Jr. *J. Chem. Phys.* **1975**, *63*, 3682.
- (5) Hamilton, E. J., Jr.; Lii, R.-R. *Int. J. Chem. Kinet.* **1977**, *9*, 875.
- (6) DeMore, W. B. *J. Phys. Chem.* **1979**, *83*, 1113.
- (7) Cox, R. A.; Burrows, J. P. *J. Phys. Chem.* **1979**, *83*, 2560.
- (8) Lii, R.-R.; Sauer, M. C., Jr.; Gordon, S. J. *Phys. Chem.* **1981**, *85*, 2833.
- (9) Kircher, C. C.; Sander, S. P. *J. Phys. Chem.* **1984**, *88*, 2082.
- (10) Lii, R.-R.; Gorse, R. A., Jr.; Sauer, M. C., Jr.; Gordon, S. J. *Phys. Chem.* **1980**, *84*, 813.
- (11) Andersson, B. Y.; Cox, R. A.; Jenkin, M. E. *Int. J. Chem. Kinet.* **1988**, *20*, 283.
- (12) Bloss, W. J.; Rowley, D. M.; Cox, R. A.; Jones, R. L. *Phys. Chem. Chem. Phys.* **2002**, *4*, 3639.
- (13) Sander, S. P.; Peterson, M. J. *Phys. Chem.* **1984**, *88*, 1566.
- (14) Christensen, L. E.; Miller, C. E.; Sloan, J. J.; Okumura, M.; Sander, S. P. *J. Phys. Chem. A* **2003**, *108*, 80.
- (15) Aloisio, S.; Francisco, J. S.; Friedl, R. R. *J. Phys. Chem.* **2000**, *104*, 6597.
- (16) Nelander, B. *J. Phys. Chem. A* **1997**, *101*, 9092.
- (17) Hamilton, E. J., Jr.; Naleway, C. A. *J. Phys. Chem.* **1976**, *80*, 2037.
- (18) Aloisio, S.; Francisco, J. S. *J. Am. Chem. Soc.* **2000**, *122*, 9196.
- (19) Curtiss, L. A.; Frurip, D. J.; Blander, M. J. *Chem. Phys.* **1979**, *71*, 2703.
- (20) Feyereisen, M. W.; Feller, D.; Dixon, D. A. *J. Phys. Chem. A* **1996**, *100*, 2993.
- (21) NIST Standard Reference Database Number 69 (June 2005 release); 2005.
- (22) Stone, D.; Rowley, D. M. *Phys. Chem. Chem. Phys.* **2005**, *7*, 2156.
- (23) Pimentel, G. C.; McClellan, A. L. *The Hydrogen Bond*; W. H. Freeman and Company: San Francisco, 1960.
- (24) Aloisio, S.; Francisco, J. S. *J. Phys. Chem. A* **1998**, *102*, 1899.
- (25) Aloisio, S.; Li, Y.; Francisco, J. S. *J. Chem. Phys.* **1999**, *110*, 9017.
- (26) Noell, A. C.; Okumura, M.; Sander, S. P. Private communication, 2006.
- (27) Curtis, A. R.; Sweetenham, W. P. *FACSIMILE/CHEKMAT*, H015 ed.; Harwell: Oxfordshire, U.K., 1987.
- (28) Sander, S. P.; Friedl, R. R.; Ravishankara, A. R.; Golden, D. M.; Kolb, C. E.; Kurylo, M. J.; Huie, R. E.; Orkin, V. L.; Molina, L. T.; Moortgat, G. K.; Finlayson-Pitts, B. J. *Chemical Kinetics and Photochemical Data for Use in Atmospheric Studies*, Evaluation No. 14, JPL 02-25; Jet Propulsion Laboratory, Pasadena, CA, 2003; web address: <http://jpldataeval.jpl.nasa.gov/>.
- (29) Rothman, L. S.; Rinsland, C. P.; Goldman, A.; Massie, S. T.; Edwards, D. P.; Flaud, J. M.; Perrin, A.; Camy-Peyret, C.; Dana, V.; Mandin, J. Y.; Schroeder, J.; McCann, A.; Gamache, R. R.; Wattson, R. B.; Yoshino, K.; Chance, K. V.; Jucks, K. W.; Brown, L. R.; Nemtchinov, V.; Varanasi, P. J. *Quant. Spectrosc. Radiat. Transfer* **1998**, *60*, 665.
- (30) Pickett, H. *MOIAM* (program to compute internal rotation structural parameters); Herbert Pickett at The Jet Propulsion Laboratory: Pasadena, CA, 2005.
- (31) Xantheas, S. S.; Dunning, T. H. *J. Chem. Phys.* **1993**, *99*, 8774.
- (32) Xiang, T.; Torres, M. L.; Guillory, W. A. *J. Chem. Phys.* **1985**, *83*, 1623.
- (33) Kanno, N.; Tonokura, K.; Tezake, A.; Koshi, M. *J. Phys. Chem. A* **2005**, *109*, 3153.
- (34) Lendvay, G. Z. *Phys. Chem.* **2001**, *215*, 377.